

Analysis and Design Techniques Applied to Hybrid Vehicle Drive Machines—Assessment of Alternative IPM and Induction Motor Topologies

David G. Dorrell, *Senior Member, IEEE*, Andrew M. Knight, *Senior Member, IEEE*, Lyndon Evans, and Mircea Popescu, *Senior Member, IEEE*

Abstract—In this paper, different analysis and design techniques are used to analyze the drive motor in the 2004 Prius hybrid vehicle and to examine alternative spoke-type magnet rotor (buried magnets with magnetization which is orthogonal to the radial direction) and induction motor arrangements. These machines are characterized by high transient torque requirement, compactness, and forced cooling. While rare-earth magnet machines are commonly used in these applications, there is an increasing interest in motors without magnets, hence the investigation of an induction motor. This paper illustrates that the machines operate under highly saturated conditions at high torque and that care should be taken when selecting the correct analysis technique. This is illustrated by divergent results when using I-Psi loops and dq techniques to calculate the torque.

Index Terms—AC drive, brushless permanent-magnet (PM) motor, hybrid electric vehicle (EV) (HEV), induction motor.

I. INTRODUCTION

A. Background

THIS PAPER reports on a study into the performance of interior permanent-magnet (PM) (IPM) drive motors and an alternative copper-cage induction machine (IM). It highlights the methods and techniques used in their analyses. The design data for the IPM are taken from a report on the 2004 Toyota Prius and the 2007 Toyota Camry hybrid electric vehicle (EV) (HEV) drive [1]. The compared spoke-type IPM (circumferentially magnetized buried magnets as described in [27] and [30] and several other treatises on PM motors) and IM drive designs use a similarly dimensioned stator design to the 2004 Prius simply because it is the most common machine in production. The Camry drive motor is actually very similar in its arrangement and dimensions with changes to the winding and IPM rotor which increase its efficiency by a very few

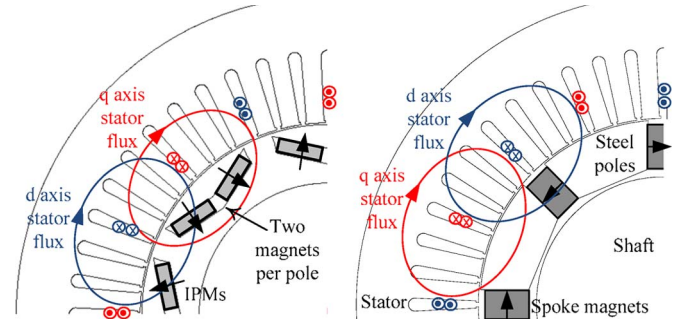


Fig. 1. 2004 Prius (left) IPM motor cross section and (right) alternative spoke-type IPM in *SPEED* PC-BDC—This shows two magnets per pole for the Prius motor, one magnet per pole for the spoke-type IPM, and high saliency in both cases).

percent. In high-efficiency machines, this will have a substantial effect, and this will be discussed later.

There is a common perception that the PM motor is the correct solution for the application and offers considerable advantages in terms of performance and efficiency. However, there is little information that has been published comparing side-by-side performance of equivalent designs. This is despite the fact that IMs have been used to drive a number of vehicles, including the General Motors EV1 and the Tesla sports car [2] (EVs). Given that the future world supply of rare-earth magnet material may be restricted [3], then it is worth considering optional arrangements, and the induction motor does have advantages over its PM counterpart in terms of material and manufacturing costs and durability. When it is required to freewheel, it will offer energy saving in terms of removal of excitation and, hence, iron loss.

Switched reluctance machines have also been studied as alternatives [4]–[7], and these are now being designed with high efficiency and, again, offer unexcited freewheeling.

The 2004 Prius machine design was studied in [7] and [8], and comparisons were made to first-pass designs for induction and switched reluctance machines. In this paper, the induction motor design is refined, and a spoke-type magnet IPM machine design, shown in Fig. 1, is introduced.

B. Literature Review

There have been many recent studies into the power control in hybrid vehicle systems [9]–[14]. Indeed, there have been several research studies into energy storage and management

Manuscript received January 5, 2011; revised June 17, 2011; accepted August 8, 2011. Date of publication August 22, 2011; date of current version April 27, 2012.

D. G. Dorrell is with the School of Mechanical, Electrical and Mechatronic Systems, University of Technology Sydney, Sydney, NSW 2007, Australia (e-mail: ddorrell@eng.uts.edu.au).

A. M. Knight is with the Department of Electrical and Computer Engineering, University of Alberta, Edmonton, AB T6G 2V4, Canada (e-mail: knight@ece.ualberta.ca).

L. Evans and M. Popescu are with the Motor Design Ltd., SY12 9DA Ellesmere, U.K. (e-mail: lyndon.evans@motor-design.com; mircea.popescu@motor-design.com).

Color versions of one or more of the figures in this paper are available online at <http://ieeexplore.ieee.org>.

Digital Object Identifier 10.1109/TIE.2011.2165460

for these vehicles [15]–[18], effects on power systems [19]–[21], and fuel resourcing [22]. At the heart of these systems is the electromechanical energy conversion. Various drives of unusual topology have been reported upon [23], [24]; however, these are still development topologies. The standard arrangement of radial-flux slotted-stator machine is still the most prevalent type of motor in production since it has been refined and studied for many years. The IPM arrangement as used by Toyota [1] could be replaced by a spoke-type magnet arrangement. Laskaris and Kladas [25] studied a spoke IPM motor for hybrid vehicle application, and in this paper, it is directly compared to the 2004 Prius machine. As previously mentioned, induction motors have been applied to EVs [2]; studies have been carried out on specialized rotor configurations for cage induction motor drives for hybrid vehicles [26]. This paper will use a more standard arrangement in order to assess their suitability in a known application.

C. Methodology

A *SPEED* model [27] using PC-BDC (an analytical calculation package from the *SPEED* Laboratory, University of Glasgow, Glasgow, UK, which uses magnetic circuits with embedded finite-element-analysis (FEA) capabilities) for the existing 2004 Toyota Prius drive motor was developed and validated using the performance data in [1]. Detailed analysis and results were put forward in [7] and [8], and these are reviewed here for completeness together with a study on a spoke-type IPM rotor.

An initial induction motor design was developed in *SPEED* PC-IMD for direct simulation comparison. Two-dimensional FEA (time stepped) models for the IM were also developed to predict torque, loss, and efficiency to a more accurate detail. This study was reported in [7] and [8], and here, an improved IM design is put forward and compared. The time-stepped FEA was carried out using JMAG from JSOL Corporation, Japan.

Basic thermal analysis was presented in [8] for the IM. Sophisticated thermal analysis techniques are now available [28]. Forced cooling with water or oil is used in these machines [29] so that it is possible to control the temperature in a similar manner to temperature control of the HEV internal combustion engine, but there will be a limit to the amount of cooling that is possible. Thermal analysis of EV and HEV drive motors is critical to successful operation. These have very high current density and rapid temperature rises, hence they require forced fluid cooling [29].

Efficiency plots, which are a new technique that is being more extensively used in motor analysis, were reported for the Prius machine in [8], and these show that it is often over 90% for the *SPEED* PC-BDC model and well over 80% for most of its operation. These correspond to the results in [1] and [29]. This is reviewed hereinafter.

Common limits for the torque per rotor volume (TRV) in various machines were quoted in [30], and these are listed in Table I.

The drive motors addressed in this paper push the envelope for these limits. In totally enclosed fan-cooled machines, typical winding current density levels are in the region of 5–6 A/mm².

TABLE I
TYPICAL TRVs [30]

Motor Type	TRV (kNm/m ³)
Fractional TEFC industrial motors	1.4 – 4
Integral TEFC industrial motors	15 – 30
High-performance industrial servos	20 – 45
Aerospace machines	45 – 75
Very large liquid-cooled machines	130 – 220

Larger water- or oil-cooled machines can push this much higher. In EV and HEV drive motors, the peak power rating is a transient rating at lower speeds, and the current density during a transient (or acceleration) period can be in excess of 20 A/mm² for a period of several seconds or tens of seconds. Even with these high-current densities, the efficiency is still high, and the cooling can be controlled via the water or oil cooling system.

II. 2004 PRIUS PM MOTOR ANALYSIS

A. Basic *SPEED* PC-BDC Models of IPM Machines

A *SPEED* PC-BDC model [4] was developed based on the specifications given in [1] and passed through to the finite-element bolt-on package *SPEED* PC-FEA. The machine has complicated rotor geometry, with reluctance torque, so it is important to cross check and compare results. This was done extensively in [8]. A lamination cross section taken from this data is shown in Fig. 1. In addition, a spoke-type IPM version is shown as an alternative arrangement. This contains the same amount of magnet material and retains the same stator and inner and outer rotor diameters. Reference [1] presents some test results which can be used to validate the *SPEED* motor model for the IPM. The test results in [1] are couched in terms of efficiency maps with torque/speed axes and efficiency contours which appear to give the limits of operation. Torque, maximum efficiency, and speed information taken from this data are plotted in Fig. 2, together with the simulation results from *SPEED* PC-BDC/FEA.

B. Operating Current Angle

As is common for IPM machines, this machine has significant inverse saliency, with the q -axis inductance larger than the d -axis inductance. The torque is written as [30]

$$T = \frac{3p}{2} (\lambda_{pm} i_q + (L_d - L_q) i_d i_q) \quad (1)$$

where the first bracketed term is the excitation torque and the second is the reluctance torque. It is obvious (and well known) that reluctance torque may be exploited by applying a negative d -axis current component. For a given magnitude current \hat{I} , the q -axis and d -axis currents may be written as

$$i_{q,d} = \hat{I} [\cos \gamma, \sin \gamma] \quad (2)$$

where γ is the “angle of advance,” which is the angle of the current vector in advance of the q -axis. If the machine is not saturated, (1) may be written as

$$T = \frac{3p}{2} (\lambda_{pm} \hat{I} \cos \gamma + (L_d - L_q) \hat{I}^2 \sin \gamma \cos \gamma). \quad (3)$$

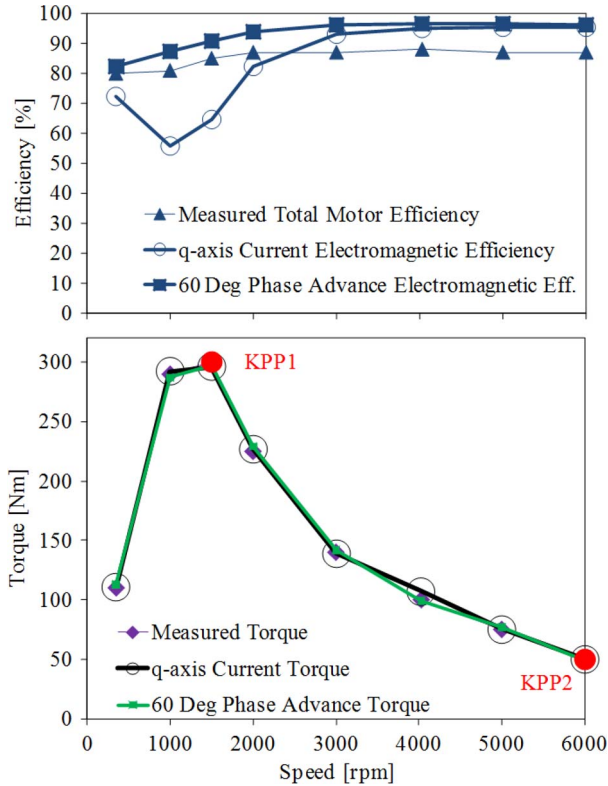


Fig. 2. Comparison of 2004 Prius *SPEED* PC-BDC operating envelope with those published in [1] showing good agreement. Control maintains current on q -axis, and 60° phase advance and full I-Psi loops are used to obtain the torque, iron loss, and efficiency (x -axis scales are the same).

This familiar torque equation suggests that maximum excitation torque occurs at an angle of advance of zero and that the maximum reluctance torque occurs at 45° angle of advance. Depending on the specific machine design, it is expected that the maximum total torque occurs with an angle of advance somewhere between 0° and 45° .

However, if the machine is normally saturated, increasing the angle of advance will reduce both the q -axis and the d -axis saturation. As the q -axis current (and flux) is reduced, L_q will increase, while field weakening current may reduce the d -axis saturation and allow λ_{pm} to increase. As a result, the angle of advance at which maximum torque is obtained may be significantly higher than expected from linear analysis. This is illustrated later.

The machine is believed to operate with a 60° phase advance (see later results); however, it is unclear from the results in [1] whether they used this phase advance on their test rig. Therefore, simulations were run with current on the q -axis and 60° advanced. The simulations will produce higher efficiencies than the measurements because additional friction and windage losses of the motor and load are not included.

It should be noted that, since the work in [7] and [8] was conducted, the *SPEED* software has been upgraded to allow for more complete and efficient simulation, particularly, of the iron loss. Results in [7] and [8] used single-point saturable torque calculations using the dq axis theory for initial torque point calculation over the speed range. The machine is highly saturated at maximum torque operation and q -axis current so

that there is a divergence between torque calculations. To obtain more accurate torque calculation, a full current-flux linkage (I-Psi) loop should be used which is what is done in Fig. 2 here. Therefore, the results in Fig. 2 are improved results from [8]. I-Psi loops are investigated further hereinafter. The temperatures of the machine were locked to 100°C for the magnets and windings and 80°C for the air gap.

It can be clearly seen that the 60° phase advance (which is often used for field weakening) is actually improving the performance at low speed. This is due to the reluctance torque of the machine. The machine appears to have a base speed of 1500 r/min and a peak speed of 6000 r/min. The efficiency data shown in Fig. 2 show little variation at the correct phase advance, with high efficiency over the full speed range. It is clear that eliminating d -axis current will prevent the exploitation of reluctance torque. To fully exploit the full torque capability of the machine, negative d -axis current will be needed. With 60° phase advance, the efficiency characteristic follows a similar trajectory, but the efficiency is constantly several percent higher. This could be because the true steel is unknown (which could raise the iron loss), but more likely, *SPEED* is calculating the electromagnetic efficiency, whereas the experiments measure true efficiency (as already mentioned) so there is no calculated friction and windage. This machine runs with coolant flowing in the air gap; this is likely to raise mechanical losses.

It should be borne in mind that the critical range for this type of machine is from 0 up to about 2000 r/min. This is where best usage of the hybrid energy system will be obtained during the urban cycle and where there will be most demand on the drive with almost continuous acceleration-deceleration which could be close to maximum torque. In Fig. 2, two points are indicated as the key point performance indicators (KPP1 and KPP2). KPP1 has most bearing on the urban cycle and overall vehicle performance, while KPP2 is less important and is likely only to affect the top speed of the vehicle, which is often in excess of normal driving speeds.

At KPP1, the rms current density is 40 A/mm^2 with the current on the q -axis (see later) which is excessively high, even for a forced fluid cooling system. With 60° phase advance, it is 17.1 A/mm^2 which is more acceptable and within normal bounds of fluid-cooled machine. This illustrates the need for phase advance.

C. I-Psi Loops and Loss Data

Inspection of Fig. 1 shows that the teeth and stator yoke are relatively wide when compared to the slot opening. This design is necessary due to the high flux levels when the machine is heavily loaded. Even so, the machine is still heavily saturated under certain conditions. To study the machine with phase advance, the PC-BDC/FEA model is evaluated further using the I-Psi loop method at two speeds: 1500 and 6000 r/min using KPP1 and KPP2. To further highlight the difference in performances predicted using the two simulation packages, the loss data with 0° (on the q -axis) and 60° phase advances at KPP1 and KPP2 are given in Table II. These represent the effective base speed and peak speed. In addition, the current density, phase voltage, and power factors are noted. The

TABLE II
2004 PRIUS PM MOTOR WITH AND WITHOUT FIELD WEAKENING AT
1500 AND 6000 r/min USING I- Ψ I LOOPS (CORRECTED FROM [8])

Speed [rpm]	1500	
Current angle w.r.t q axis	0°	60°
Torque [Nm]	296	297
Line Current (rms) [A]	339	145
Power Factor	0.28	0.71
Cu Loss [W]	24931	4547
Fe Loss [W]	358	202
Efficiency [%]	64.7	90.8
Current Density [A/mm ²]	40	17.1
Speed [rpm]	6000	
Current angle w.r.t q axis	0°	60°
Torque [Nm]	50.5	49.2
Line Current (rms) [A]	35.4	35.4
Power Factor	0.55	0.98
Cu Loss [W]	270	270
Fe Loss [W]	2997	969
Efficiency [%]	95.3	96.1
Current Density [A/mm ²]	4.16	4.16

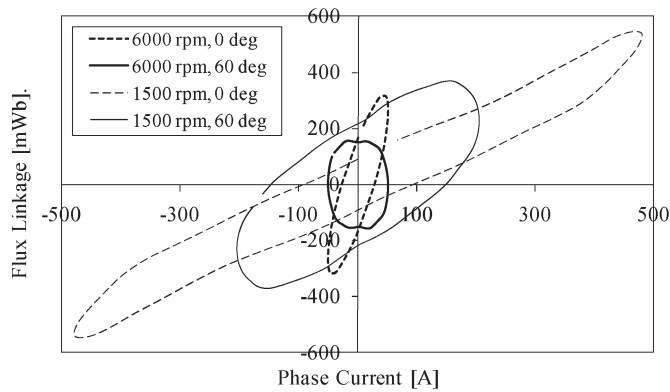


Fig. 3. I- Ψ loops or diagrams for the PC-FEA points in Table II.

currents are adjusted to obtain the correct torques. In [8], detailed descriptions of different torque calculation methods were put forward, but here, only the I- Ψ i loops are used to calculate the machine flux in PC-FEA and give more accurate torque and loss. These are extensively used for torque prediction in switched reluctance machines, but they can be used in many types of machine [31]. Loops for each of the four points in Table II are shown in Fig. 3. The area enclosed represents the work done in one cycle of the current, and this can be used to obtain the mean torque per phase using the speed. For three-phase machines, all three phases will trace out a similar ellipse, allowing a multiplier of three to be used for the total torque. This is a powerful technique for calculating torque. The power factor in Table II is calculated by summing the mechanical power and the losses and dividing by total voltamperes. This will then take into account any distortion factor. The phase voltage waveforms as obtained from 45 points round the I- Ψ i loops are shown in Fig. 4 (60° phase advance).

It can be seen that the most significant source of losses changes from copper loss at 1500 r/min to iron loss at 6000 r/min and that the current density is high at maximum torque (300 N · m). The steel used was M19-24 gauge steel, while this may not be the precise steel used (since, at 6000 r/min, the line frequency is 400 Hz which is an aero-

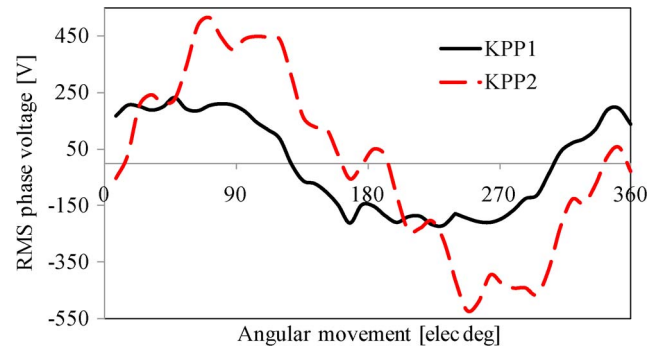


Fig. 4. Terminal voltages from PC-FEA I- Ψ i loops: KPP1 (1500 r/min, 60° advance, and 145 A rms) and KPP2 (6000 r/min, 60° advance, and 34.5 A rms).

TABLE III
COMPARISON OF PM AND INDUCTION MOTORS

Parameter	PM Motor	IM (1 st Pass Design)	IM (Improved Design)
Outer stator diameter [mm]	269.0	269.0	270
Inner rotor diameter [mm]	111.0	111.0	110
Outer rotor diameter [mm]	160.5	180.0	180
Air-gap length [mm]	0.73	1.5	0.5
Axial core length [mm]	84	84	84
Weight of stator core [Kg]	18.65	11.86	---
Weight of stator copper [Kg]	5.99	10.57	---
Weight of rotor core [Kg]	5.22	6.15	---
Weight of rotor magnet/copper [Kg]	1.30	7.67	---
Lamination material	M19 – 24 gage	M19 – 24 gage	35JN440
Skew	none	1 rotor slot	none

nautical system frequency level); it appears to give reasonable correlation.

D. TRV

The rotor has a volume of 0.0017 m³ (the dimensions are given in Table III, allowing comparison with an induction motor design). Therefore, using 300 N · m as the peak rating at 1500 r/min gives a TRV of 175 kN · m/m³. From Table I, it can be seen that this is well into the range for very large fluid-cooled machines. However, this is a transient situation, and it is not expected that the machine will operate continuously at this power and speed. At 50 N · m, the TRV is 29.4 kN · m/m³. The machine may well be expected to operate at maximum power at maximum speed in a more continuous mode.

E. Flux and Iron Loss Distribution

The flux density and iron loss distributions for the machine at the 6000 r/min point and full power are shown in Fig. 5. This is with 60° phase advance ([8] kept the current on the q-axis). Similar data are shown in Fig. 6 for the case at 1500 r/min. The currents in the 1500-r/min case are at 145 A, rather than the 35.4 A used in the 6000-r/min simulation. The flux density plots show that the flux is significantly lower at 6000 r/min and full power even though, as shown in Table II, the iron loss is much higher than that of the maximum-torque 1500-r/min case.

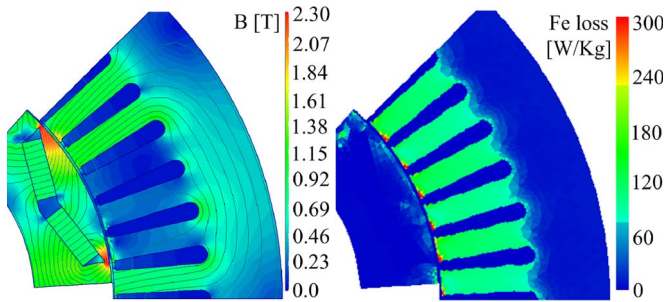


Fig. 5. (Left) Flux density and (right) iron loss distributions at 6000 r/min with 34.5 A rms and 60° phase advance.

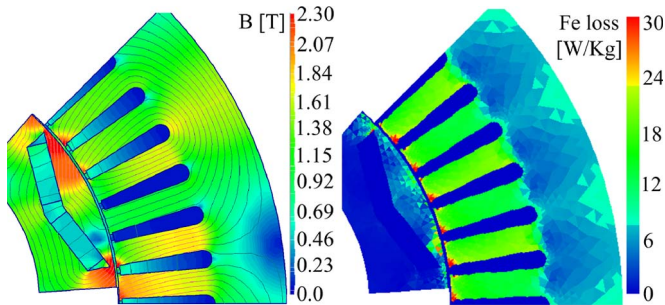


Fig. 6. (Left) Flux density and (right) iron loss distributions at 1500 r/min with 145 A rms and 60° phase advance.

This difference occurs obviously because the flux alternates at 400 Hz at 6000 r/min and 100 Hz at 1500 r/min—The decrease in flux density is more than offset by the increase in fundamental frequency. At high speed, iron losses can be very substantial and cannot be neglected in the motor design.

To obtain the iron losses in the FEA, the elemental flux over one cycle is obtained, and a modified Steinmetz equation [32] is used to predict the iron losses based on the manufacturer steel data. It should be noted that the actual machine losses may vary from the predictions due to uncertainty regarding the actual steel grade used in the machine. Most of the iron loss is in the stator teeth and that, as expected, rotor iron losses are minimal.

F. Efficiency Plots

In [1], efficiency plots were used to illustrate the motor operation, and these can be obtained from simulations too. Fig. 7 shows the efficiency plot for the machine using PC-BDC with the FEA internal calculation tool option selected. This was included in [7] and [8] but is again included here for completeness. For a brushless PM motor, then, there are several parameters that can be set. In this case, at each load point, the phase angle advance was set at 0°, 30°, and 60°, and the current varied until the correct torque was obtained. The highest efficiency was then selected as the operating point. The selected phase angle is shown in the top chart while the efficiencies are shown as colored regions and contour lines in the bottom plot. The PC-BDC efficiency plot is shown here simply as an example. The efficiencies are high because there is no friction and windage loss included (which was measured as being up to 1 kW in [1] and 6000 r/min and could be even higher with the forces

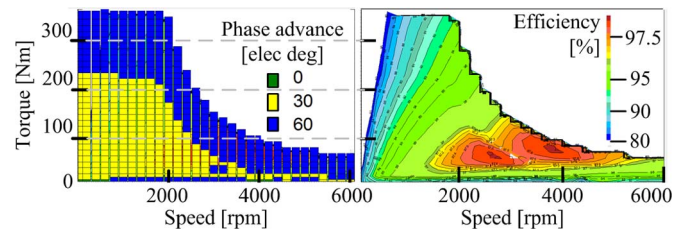


Fig. 7. Efficiency plot for PC-BDC/FEA simulations using phase angles of 0°, 30°, and 60°. Torque is calculated using the dq method outlined hereinafter.

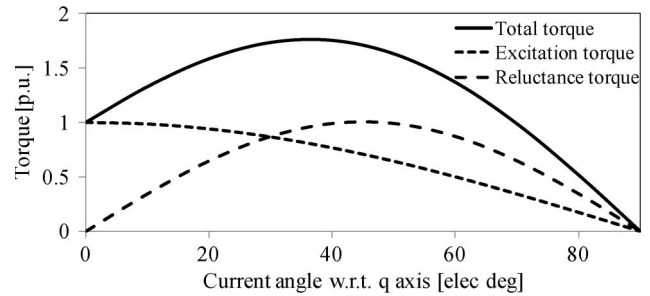


Fig. 8. Idealized torque variation for q -axis saliency in an IPM machine.

cooling under load as discussed earlier). A similar exercise can be conducted using any motor calculation tool that allows automated and repeated simulations over a range of parameter range variations. *SPEED* software is scriptable under Windows ActiveX, and it is straightforward to generate scripts in, for instance, Visual Basic, MATLAB, or, as in this case, Delphi T-Chart, to carry out this sort of exercise.

G. Different Torque Calculations and Frozen Permeability Method

As can be seen in Fig. 1, there is substantial q -axis saliency in this machine. Reference [1] conducted a locked-rotor dc current test that shows considerable reluctance torque in addition to the excitation torque. To reduce the current density and improve the power factor, phase advance can be used as discussed earlier. To assess the different components due to the excitation torque and reluctance torque, the “frozen permeabilities” method [33] may be applied. Here, the machine is solved as a complete solution, and the calculated nonlinear magnetic permeabilities are locked and stored. Different magnetomotive force sources can then be excited, in turn, with constant permeabilities from the full solution to find different components of flux and torque. In this case, the magnet excitation can be removed to find the reluctance torque. The excitation torque is then calculated as the difference between the total and reluctance torques. For a machine with q -axis saliency, then, the idealized torque components are shown in Fig. 8 where the excitation and reluctance torques peak at 1 p.u. and vary in a sinusoidal manner. Predictions for torque components at 1500 and 6000 r/min with two different current levels are shown in Fig. 9. It can be seen that the reluctance torque changes in shape and magnitude due to saturation.

The frozen permeability method can be used using the I-Psi loops; however, here, it was decided to test other torque

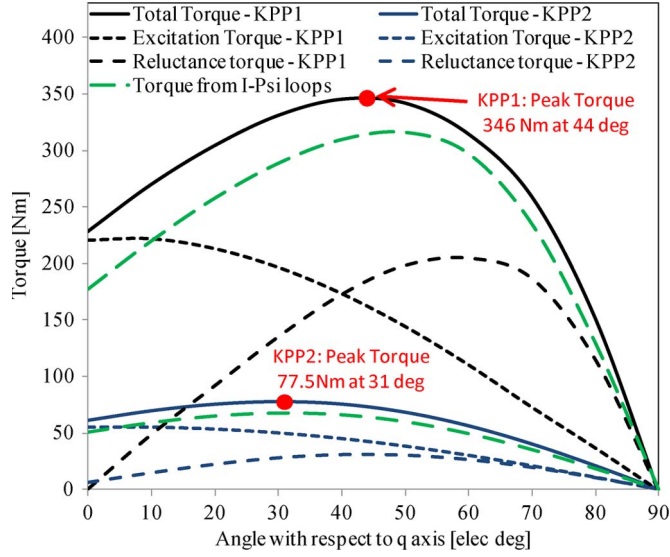


Fig. 9. Separation of torque at KPP1 (1500 r/min, 145 A) and KPP2 (6000 r/min, 35.4 A) loading using dq torque calculation method—variation of current phase with respect to q axis. I-Psi calculation is included for comparison.

calculation methods for comparison. Therefore, the frozen permeability method was applied using the dq equation [30]

$$T = 3p(\Psi_d I_q - \Psi_q I_d) \quad (4)$$

where p is the pole-pair number. In the FEA simulation, the rotor is locked, and the current vector is rotated to give variation of the d and q components of the current; also, the flux linkage Ψ of the winding is measured and resolved into the d and q components. This is much faster than the I-Psi loops but prone to more error. It can be seen that there is a reasonably large difference in the torque obtained from the I-Psi loops and from (1) which increases with torque (and saturation). It is often advisable to check the torque using more than one method of calculation.

These results give target performance figures for a possible spoke-type IPM and IM replacements; these are investigated in the next sections. While the current densities seem high at low speed, these are on the maximum torque/speed envelope for the machine and are transient during motor acceleration (and possible regeneration). The motor is cooled via a fluid cooling system. For consistency, the machine windings and magnet were set at 100 °C.

III. COMPARISON TO SPOKE-TYPE MOTOR

In the previous section, the 2004 Prius IPM motor was examined in great detail. The 2007 Camry drive motor was also described in [1]. This machine was also a high-performance machine of a similar topology, but it was reported to be about 3% more efficient, so it is possible to improve the performance of machines of this ilk even when they are already very efficient. In this section, comparison is made to the spoke IPM machine shown in Fig. 1. The torque is compared directly (using I-Psi loops for accuracy) at KPP1 and KPP2. At KPP1, the current is kept constant at 145 A, while it is kept constant at 35.4 A at

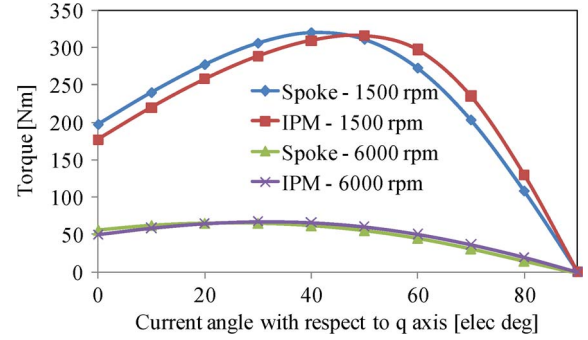


Fig. 10. Comparison for IPM and spoke-type motor torques in Fig. 1 at KPP1 and KPP2 with the same currents.

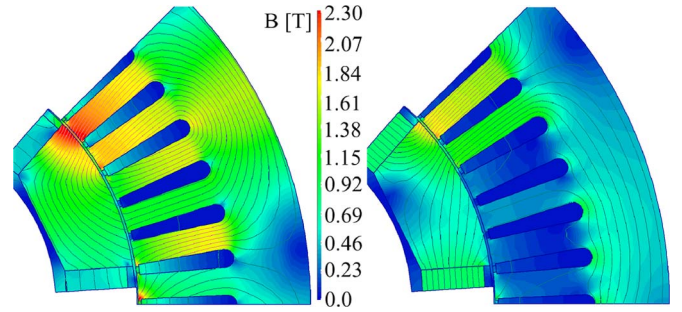


Fig. 11. Flux plots for spoke-type machine at (left) KPP1 and (right) KPP2; same flux density scale for both.

KPP2. The results with variation of current phasor with respect to the q -axis are shown in Fig. 10. It can be seen that the spoke-type motor has a slightly different profile but offers a similar performance. The copper loss is constant, and the iron losses are similar. This is a first-pass arrangement, and the amount of magnet is kept constant. Flux plots for KPP1 and KPP2 are shown in Fig. 11. The phase advance is 60° in both instances.

IV. INDUCTION MOTOR DESIGN

In this section, an induction motor design is considered. In [8], a 53-bar rotor was considered together with a 40-bar adjustment to aid time-stepped FEA (allowing 5-bar periodicity rather than whole motor simulation). The first-pass design was designed using the analytical simulations in *SPEED* PC-IMD, but to allow for more accuracy in calculation, only time-stepped (or transient) FEA is reported here so that the 40-bar design is focused upon. The eight-pole arrangement is maintained—further work would be to compare other pole number IMs to the eight-pole arrangements used here.

A. Design Comparison

The general dimensions for the PM motor are taken as the basis for an induction motor design. Because the flux levels can be adjusted, then it is possible to adjust the tooth width in the stator and the yoke thickness. In addition, the rotor diameter can be increased in order to improve the torque-arm length and also allow deeper rotor slots. The inner rotor diameter, outer stator diameter, and axial length are taken as being set by the application. Table III gives the dimensions of the first-pass induction motor design and the improved design compared

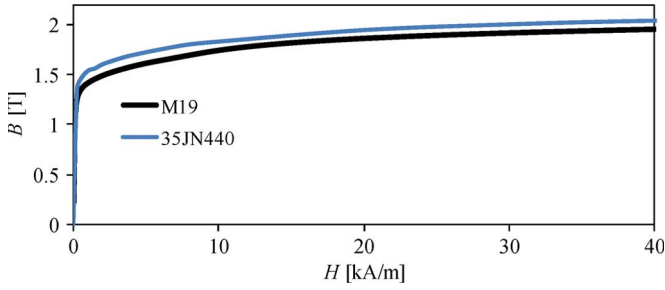


Fig. 12. Comparison of IM steels.

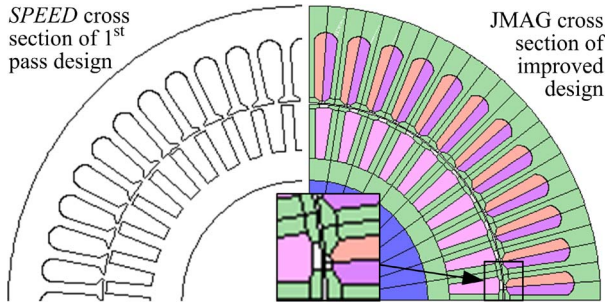


Fig. 13. Cross sections for (left) original IM and (right) improved design.

to the PM motor design. The improved IM design uses higher flux steel as shown in Fig. 12. Cross sections of the first pass and improved IM are shown in Fig. 13. This design maintains the eight-pole 48-stator-slot arrangement. For the time-stepped FEA analysis, 40 bars were used simply to afford a degree of symmetry and allow a one-pole periodicity (as discussed earlier). The windings in the induction motor were rearranged in terms of series/parallel connection although the wire gauge and slot fill were maintained. The first-pass design has one stator slot skew. However, this was removed in the improved design in order to improve the linkage.

In the simulations, the stator and rotor conductors were set at 100 °C for direct comparison to the PM machine. Table II also indicates that there is substantial open-circuit iron loss in the PM machine at high speed, which will not occur in the induction motor.

B. Transient FEA

A time-stepped FEA model has been used to further investigate the IM designs. For the first-pass design, the time-stepped model uses five slices to model a skew that is equal to one bar slot pitch. Data from predictions at 1475 and 5960 r/min are given in Table IV. It can be seen that the time-stepped FEA predicts low power factor and high losses in the low-speed case, where the machine is very saturated. This may be due to eddy current redistribution, slotting, and skew. The rotor bar slots are open (Fig. 13), and the air-gap length is quite long at 1.5 mm (it was initially envisaged that a long air-gap length would allow high electrical loading and reduce slotting effects). Fig. 14 shows the eddy current density for one instant of the time-stepping solutions. It can be seen that, while the bulk current density in the bars is of the same order as in the

TABLE IV
TIME-STEPPED FEA PREDICTIONS OF PERFORMANCE FOR A SKEWED ROTOR WITH 40 ROTOR BARS AND 48 STATOR SLOTS

Actual/synchronous speeds [rpm]	1475/ 1548	5960/6000
Simulation method	1 st pass design	Improved design
Torque [Nm]	300	270
Line current (rms) [A]	238.4	147.4
Line voltage (rms) [V]	350	306
Power Factor	0.45	0.63
Stator Cu loss [W]	13174	5211
Rotor Cu loss [W]	3778	2852
Fe loss [W]	418	---
Efficiency [%]	71.3	83.8

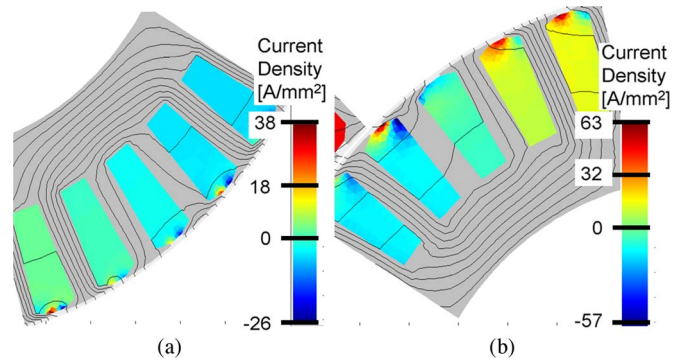


Fig. 14. Rotor bar current density showing eddy currents at slot tops. (a) 5960 r/min. (b) 1475 r/min.

initial predictions, there are regions of much higher current density near the slot tops. This will affect the linkage with the stator and the equivalent circuit of the machine. Skew will reduce the stator-rotor linkage and generate further saturation in the axial direction [34]. Therefore, it was decided to improve the design. The rotor slots were semiclosed as shown in the inset in Fig. 13, and the skew was removed. While skew is important for grid-connected machines, it is less so for inverter-connected machines such as this. The winding was maintained. Table IV shows the results at 1475 r/min with the same slip as the first-pass design, and it illustrates a good improvement in performance with the efficiency increasing from 71.3% to 83.8%.

The performance at 6000 r/min was good for the first-pass design so the improved design simulation was not carried out here. Instead, the speed and slip were maintained at 1475 r/min, and the voltage was varied to examine the improved design. Fig. 15 shows the torque and torque-per-peak-current variation at three voltage points. The torque is found to be almost proportional to the square of the voltage; however, saturation is coming into effect at these voltage levels. If there is no saturation, and the magnetization current is low, then the torque per peak current will vary linearly with voltage. However, as saturation occurs, the current increase with voltage becomes nonlinear, and the torque per peak ampere diverges from the linear characteristic as shown in Fig. 15. This shows that the 300-N·m point is about the maximum torque for this machine.

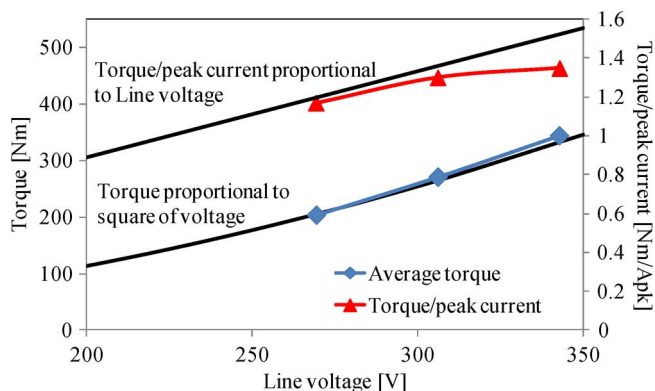


Fig. 15. Improved design at 1475 r/min with fixed slip and variation of voltage–torque and torque per peak ampere (peak).

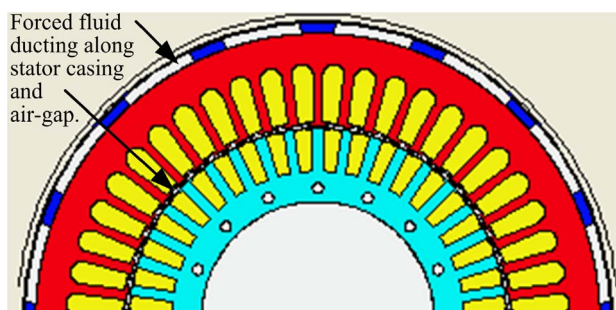


Fig. 16. MotorCAD model of the 48-slot 40-bar induction motor.

C. Transient Thermal Analysis

The induction motor is very susceptible to transient heating effects as illustrated in [28]. We can analyze the induction motor over a duty cycle to observe temperature rises. The package MotorCAD [28] was utilized to do a full thermal analysis of the first-pass-design machine over suitable duty cycles. Fig. 16 shows a MotorCAD cross section with water cooling ducts around the stator. The simulation assumes coolant fluid cooling around the stator (at 20 L/min) and also down the air gap (10 L/min). Fig. 17 shows the temperature rise for the IM studied in the time-stepping simulation at full load and 1500 r/min (using the loss data as calculated in Table IV). It illustrates the temperature rise in key motor locations. The ambient is high, and the temperature rise is shown to be 120 °C at the center of the stator winding. This temperature rise is of a similar ilk to those reported in [29] for the Prius PM motor, although at a higher level due to the larger losses. As can be seen, the temperature rise is rapid at full power and 1500 r/min, which illustrates the duty cycling nature of a vehicular drive. Successful cooling and thermal aspects are important to this application.

One point that can be noted is that the motor may be heat-dissipation limited. If the cooling system can cope with, for example, 15% of losses at 50 kW of delivered power, this implies 8.8 kW of loss dissipation (with 58.8-kW input power). If the efficiency is increased to 90% efficiency, then for 8.8 kW of loss, then the delivered power is now 79.2 kW, which is a 58.4% improvement in output power for a given cooling system. If the efficiency increases to 95%, then the output power is 167.2 kW. This illustrates that a few percent improvement in efficiency can

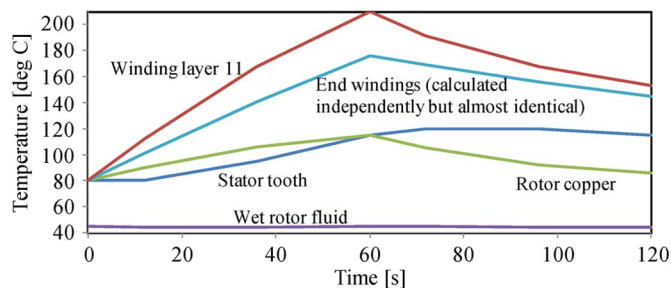


Fig. 17. Temperature rise simulation—3 min at full load and 1500 r/min.

lead to a much higher increase in output power potential for a given cooling system.

V. CONCLUSION

This paper has reviewed some of the common techniques for designing and analyzing electrical machines in the context of EV and HEV drive motors, particularly the 2004 Toyota Prius machine. These machines run at high saturation and transient thermal operation. It is apparent from this paper that the design of high-saturation machines is less straightforward than standard industrial machines. Detailed FEA needs to be used to ensure accuracy. In addition, this application requires careful thermal consideration because much of the operation will be in transient conditions.

It can be seen that the original Prius motor in the study operates with phase current at a significant angle of advance, 60° ahead of the q -axis. It can therefore be inferred that the IPM operates at a low power factor, although, at KPP1, moving from 0° to 60° phase advance improves the power factor from 0.28 to 0.71 (Table II). As a result, IMs can be seen to be a viable alternative. However, the IM design at high torque density is very sensitive to saturation, and detailed finite-element models must be used to develop a competitive design. Even, in this case, the operating flux densities are above those commonly provided in test data. There are studies that can aid the design of induction motors such as [35], [36], and many texts. Future research into the behavior of highly saturated steels would significantly contribute to further work in this area. In addition, other magnetless machines such as the switched reluctance machine [37] are being considered, and more novel PM machines such as the flux-switching machine [38], [39] are assessed for use in electric and hybrid vehicles. For more standard radial-flux IPM designs, multimagnet-layer arrangements [40] may also be relevant. These also have substantial q -axis saliency.

REFERENCES

- [1] M. Olszewski, "Evaluation of the 2007 Toyota Camry hybrid synergy drive system," Oak Ridge Nat. Lab., U.S. Dept. Energy, Oak Ridge, TN, 2009.
- [2] M. Eberhard, "How electric vehicles must change the way the auto industry thinks," presented at the Plenary Session, IEEE ECCE Conf., San Jose, CA, Sep. 24–28, 2009.
- [3] R. McCormack, "China's complete control of global high-tech magnet industry raises U.S. National Security Alarms," *Manuf. Technol. News*, vol. 16, no. 16, Sep. 30, 2009.
- [4] Y. Takano, M. Takeno, T. Imakawa, A. Chiba, N. Hoshi, M. Takemoto, and S. Ogasawara, "Torque density and efficiency improvements of a

- Switched Reluctance Motor without rare earth material for hybrid vehicles," in *Proc. IEEE ECCE*, Atlanta, GA, Sep. 2010, pp. 2653–2659.
- [5] Y. Takano, M. Takano, N. Hoshi, A. Chiba, M. Takemoto, S. Ogasawara, and M. A. Rahman, "Design and analysis of a switched reluctance motor for next generation hybrid vehicle without PM materials," in *Proc. IPEC*, Sapporo, Japan, Jun. 21–24, 2010, pp. 1801–1806.
 - [6] X. D. Xue, K. W. E. Cheng, T. W. Ng, and N. C. Cheung, "Multi-objective optimization design of in-wheel switched reluctance motors in electric vehicles," *IEEE Trans. Ind. Electron.*, vol. 57, no. 9, pp. 2980–2987, Sep. 2010.
 - [7] D. G. Dorrell, M. Popescu, L. Evans, D. A. Staton, and A. M. Knight, "Comparison of different motor design drives for hybrid electric vehicles," in *Proc. IEEE ECCE*, Atlanta, GA, Sep. 2010, pp. 3352–3359.
 - [8] D. G. Dorrell, M. Popescu, L. Evans, D. A. Staton, and A. M. Knight, "Modern electrical machine analysis and design techniques applied to hybrid vehicle drive machines," in *Proc. IEEE ISIE*, Bari, Italy, Jul. 4–7, 2010, pp. 3728–3733.
 - [9] Z. Amjadi and S. S. Williamson, "A novel control technique for a switched-capacitor-converter-based hybrid electric vehicle energy storage system," *IEEE Trans. Ind. Electron.*, vol. 57, no. 3, pp. 926–934, Mar. 2010.
 - [10] M. Baïlo Camara, H. Gualous, and F. Gustin, "DC/DC converter design for supercapacitor and battery power management in hybrid vehicle applications—Polynomial control strategy," *IEEE Trans. Ind. Electron.*, vol. 57, no. 2, pp. 587–597, Feb. 2010.
 - [11] Y. Gao and M. Ehsani, "Design and control methodology of plug-in hybrid electric vehicles," *IEEE Trans. Ind. Electron.*, vol. 57, no. 2, pp. 633–640, Feb. 2010.
 - [12] P. A. Cassani and S. S. Williamson, "Design, testing, and validation of a simplified control scheme for a novel plug-in hybrid electric vehicle battery cell equalizer," *IEEE Trans. Ind. Electron.*, vol. 57, no. 12, pp. 3956–3962, Dec. 2010.
 - [13] Z. Amjadi and S. S. Williamson, "Power-electronics-based solutions for plug-in hybrid electric vehicle energy storage and management systems," *IEEE Trans. Ind. Electron.*, vol. 57, no. 2, pp. 608–616, Feb. 2010.
 - [14] F. Luigi Mapelli, D. Tarsitano, and M. Mauri, "Plug-in hybrid electric vehicle: Modeling, prototype realization, and inverter losses reduction analysis," *IEEE Trans. Ind. Electron.*, vol. 57, no. 2, pp. 598–607, Feb. 2010.
 - [15] E. Manla, A. Nasiri, C. H. Rentel, and M. Hughes, "Modeling of zinc bromide energy storage for vehicular applications," *IEEE Trans. Ind. Electron.*, vol. 57, no. 2, pp. 624–632, Feb. 2010.
 - [16] P. Garcia, L. M. Fernandez, C. Andres Garcia, and F. Jurado, "Energy management system of fuel-cell-battery hybrid tramway," *IEEE Trans. Ind. Electron.*, vol. 57, no. 12, pp. 4013–4023, Dec. 2010.
 - [17] L. Gauchia and J. Sanz, "A per-unit hardware-in-the-loop simulation of a fuel cell/battery hybrid energy system," *IEEE Trans. Ind. Electron.*, vol. 57, no. 4, pp. 1186–1194, Apr. 2010.
 - [18] M. Montazeri-Gh and M. Soleymani, "Investigation of the energy regeneration of active suspension system in hybrid electric vehicles," *IEEE Trans. Ind. Electron.*, vol. 57, no. 3, pp. 918–925, Mar. 2010.
 - [19] A. Y. Saber and G. K. Venayagamoorthy, "Plug-in vehicles and renewable energy sources for cost and emission reductions," *IEEE Trans. Ind. Electron.*, vol. 58, no. 4, pp. 1229–1238, Apr. 2011.
 - [20] K. J. Dyke, N. Schofield, and M. Barnes, "The impact of transport electrification on electrical networks," *IEEE Trans. Ind. Electron.*, vol. 57, no. 12, pp. 3917–3926, Dec. 2010.
 - [21] A. Hajimiragha, C. A. Cañizares, M. W. Fowler, and A. Elkamel, "Optimal transition to plug-in hybrid electric vehicles in Ontario, Canada, considering the electricity-grid limitations," *IEEE Trans. Ind. Electron.*, vol. 57, no. 2, pp. 690–701, Feb. 2010.
 - [22] M. Van Wiering and R. Pop-Iliev, "Development of a dual-fuel power generation system for an extended range plug-in hybrid electric vehicle," *IEEE Trans. Ind. Electron.*, vol. 57, no. 2, pp. 641–648, Feb. 2010.
 - [23] C. Liu, K. T. Chau, and J. Z. Jiang, "A permanent-magnet hybrid brushless integrated starter-generator for hybrid electric vehicles," *IEEE Trans. Ind. Electron.*, vol. 57, no. 12, pp. 4055–4064, Dec. 2010.
 - [24] N. P. Shah, A. Dorr Hirzel, and B. Cho, "Transmissionless selectively aligned surface-permanent-magnet BLDC motor in hybrid electric vehicles," *IEEE Trans. Ind. Electron.*, vol. 57, no. 2, pp. 669–677, Feb. 2010.
 - [25] K. I. Laskaris and A. G. Kladas, "Internal permanent magnet motor design for electric vehicle drive," *IEEE Trans. Ind. Electron.*, vol. 57, no. 1, pp. 138–145, Jan. 2010.
 - [26] W. Li, J. Cao, and X. Zhang, "Electrothermal analysis of induction motor with compound cage rotor used for PHEV," *IEEE Trans. Ind. Electron.*, vol. 57, no. 2, pp. 660–668, Feb. 2010.
 - [27] T. J. E. Miller, *SPEED's Electrical Motors*. Glasgow, U.K.: SPEED Lab., Univ. Glasgow, 2006.
 - [28] D. G. Dorrell, "Combined thermal and electromagnetic analysis of permanent magnet and induction machines to aid calculation," *IEEE Trans. Ind. Electron.*, vol. 55, no. 10, pp. 3566–3574, Oct. 2008.
 - [29] L. D. Marlino, "Report on Toyota Prius motor thermal management," Oak Ridge Nat. Lab., U.S. Dept. Energy, Oak Ridge, TN, 2005.
 - [30] J. R. Hendershot and T. J. E. Miller, *Design of Brushless Permanent-Magnet Motors*. Oxford, U.K.: Clarendon, 1994.
 - [31] D. A. Staton, R. P. Deodhar, W. L. Soong, and T. J. E. Miller, "Torque prediction using the flux-MMF diagram in ac, dc, and reluctance motors," *IEEE Trans. Ind. Appl.*, vol. 32, no. 1, pp. 180–188, Jan./Feb. 1996.
 - [32] J. Reinert, A. Brockmeyer, and R. W. A. A. De Doncker, "Calculation of losses in ferro- and ferrimagnetic materials based on the modified Steinmetz equation," *IEEE Trans. Ind. Appl.*, vol. 37, no. 4, pp. 1055–1061, Jul./Aug. 2001.
 - [33] J. A. Walker, D. Dorrell, and C. Cossar, "Flux-linkage calculation in permanent-magnet motors using the frozen permeabilities method," *IEEE Trans. Magn.*, vol. 41, no. 10, pp. 3946–3948, Oct. 2005.
 - [34] D. G. Dorrell, P. J. Holik, P. Lombard, H.-J. Thougard, and F. Jensen, "A multisliced finite-element model for induction machines incorporating inter-bar current," *IEEE Trans. Ind. Appl.*, vol. 45, no. 1, pp. 131–141, Jan./Feb. 2009.
 - [35] A. Boglietti, A. Cavagnino, and M. Lazzari, "Computational algorithms for induction-motor equivalent circuit parameter determination—Part I: Resistances and leakage reactances," *IEEE Trans. Ind. Electron.*, vol. 58, no. 9, pp. 3723–3733, Sep. 2011.
 - [36] A. Boglietti, A. Cavagnino, and M. Lazzari, "Computational algorithms for induction-motor equivalent circuit parameter determination—Part II: Skin effect and magnetizing characteristics," *IEEE Trans. Ind. Electron.*, vol. 58, no. 9, pp. 3734–3740, Sep. 2011.
 - [37] H.-C. Chang and C.-M. Liaw, "An integrated driving/charging switched reluctance motor drive using three-phase power module," *IEEE Trans. Ind. Electron.*, vol. 58, no. 5, pp. 1763–1775, May 2011.
 - [38] T. Raminosoa, C. Gerada, and M. Galea, "Design considerations for a fault-tolerant flux-switching permanent-magnet machine," *IEEE Trans. Ind. Electron.*, vol. 58, no. 7, pp. 2818–2825, Jul. 2011.
 - [39] W. Zhao, M. Cheng, W. Hua, H. Jia, and R. Cao, "Back-EMF harmonic analysis and fault-tolerant control of flux-switching permanent-magnet machine with redundancy," *IEEE Trans. Ind. Electron.*, vol. 58, no. 5, pp. 1926–1935, May 2011.
 - [40] S. Lee, Y.-S. Jeong, Y.-J. Kim, and S.-Y. Jung, "Novel analysis and design methodology of interior permanent-magnet synchronous motor using newly adopted synthetic flux linkage," *IEEE Trans. Ind. Electron.*, vol. 58, no. 9, pp. 3806–3814, Sep. 2011.



David G. Dorrell (M'95–SM'08) is a native of St. Helens, U.K. He received the B.Eng. (Hons.) degree in electrical and electronic engineering from the University of Leeds, Leeds, U.K., in 1988, the M.Sc. degree in power electronics engineering from The University of Bradford, Bradford, U.K., in 1989, and the Ph.D. degree in engineering from the University of Cambridge, Cambridge, U.K., in 1993.

He has held lecturing positions with the Robert Gordon University, Aberdeen, U.K. and the University of Reading, Reading, U.K. He was a Senior Lecturer with The University of Glasgow, Glasgow, U.K., for several years. He has been with the University of Technology Sydney, Sydney, Australia, since 2008, when he took up a post as Senior Lecturer; he has been an Associate Professor since 2009. He is also an Adjunct Associate Professor with the National Cheng Kung University, Tainan, Taiwan. His research interests cover the design and analysis of various electrical machines and also renewable energy systems.

Dr. Dorrell is a Chartered Engineer in the U.K. and a Fellow of the Institution of Engineering and Technology.



Andrew M. Knight (S'95–A'98–M'99–SM'06) received the B.A. degree in electrical and information sciences and the Ph.D. degree in electrical power from the University of Cambridge, Cambridge, U.K., in 1994 and 1998, respectively.

Since 1999, he has been with the University of Alberta, Edmonton, AB, Canada, as an Assistant Professor, where he is currently a Professor with the Department of Electrical and Computer Engineering. His research interests include efficient utilization of electrical energy, including energy conversion and storage, particularly, renewable energy and electrical machines and drives, practical aspects of analysis and design of electric machines, and modeling of nonlinear electromagnetic systems and losses in those systems.

Dr. Knight is a Professional Engineer, registered in the province of Alberta, and was the recipient of the IEEE Power and Energy Society Prize Paper Award in 2008 and two prize papers from the IEEE Industry Application Society 2008 Annual Meeting.



Lyndon Evans received the B.Sc. (Hons.) degree in computer networks from Glyndŵr University, Wrexham, U.K., in 2008.

He was qualified as a Television and Video Service Engineer in 1988 and worked in this field for over 15 years before returning to study. He is a Software Developer with Motor Design Ltd., Ellesmere, U.K., in partnership with Glyndŵr University.

Mr. Evans is a member of the Institution of Engineering and Technology and an associate member of the British Computer Society.



Mircea Popescu (M'98–SM'04) received the D.Sc. degree in electrical engineering from Helsinki University of Technology, Helsinki, Finland, in 2004.

He has more than 25 years experience in electrical motor design and analysis. He was with the Research Institute for Electrical Machines, Bucharest, Romania, Helsinki University of Technology, and the SPEED Laboratory, Glasgow University, Glasgow, U.K. Since 2008, he has been with Motor Design Ltd., Ellesmere, U.K., as the Engineering Manager. He published over 100 papers in conferences and

peer-reviewed journals.

Dr. Popescu was the recipient of the first prize Best Paper Award from IEEE Industry Applications Society, Electric Machines Committee in 2002, 2006, and 2008.